



Mixed-spin two-dimensional lattice composed of spins $\frac{1}{2}$ and 1 in a radical-Ni complex

Y. Tominaga,¹ A. Matsuo,² K. Kindo,² S. Shimono,³ K. Araki,⁴ Y. Iwasaki,⁵ Y. Hosokoshi,¹
S. Noguchi¹ ,¹ and H. Yamaguchi^{1,*} .

¹Department of Physics, Osaka Metropolitan University, Osaka 599-8531, Japan

²Institute for Solid State Physics, The University of Tokyo, Chiba 277-8581, Japan

³Department of Materials Science and Engineering, National Defense Academy, Kanagawa 239-8686, Japan

⁴Department of Applied Physics, National Defense Academy, Kanagawa 239-8686, Japan

⁵Department of Physics, College of Humanities and Sciences, Nihon University, Tokyo 156-8550, Japan



(Received 20 May 2023; accepted 14 July 2023; published 25 July 2023)

In this study, we successfully synthesized $(p\text{-Py-V-}p\text{-F})_2[\text{Ni}(\text{hfac})_2]$, a verdazyl-based complex. Molecular orbital calculations revealed the formation of a two-dimensional spin lattice composed of spin $\frac{1}{2}$ and spin 1. The magnetization curve displayed a $\frac{1}{2}$ plateau representing full polarization of spin 1. We confirm that the increase in the magnetization curve after the $\frac{1}{2}$ plateau phase largely reflects the exchange couplings forming the effective spin- $\frac{1}{2}$ ladder composed of radicals. In the low-field and low-temperature regions, the magnetic properties are primarily attributed to spin 1 with effective interactions forming a spin-1 antiferromagnetic chain. Additionally, an anomalous change in the field derivative of the magnetization curve was observed near the plateau onset.

DOI: [10.1103/PhysRevB.108.024424](https://doi.org/10.1103/PhysRevB.108.024424)

I. INTRODUCTION

The size of spins in quantum spin systems plays a pivotal role in determining their ground state. A notable example is the antiferromagnetic (AFM) Heisenberg chains, where the ground state of a spin- $\frac{1}{2}$ chain is characterized by a Tomonaga-Luttinger liquid (TLL) state, exhibiting fermionic spinon excitations. In contrast, a spin-1 chain exhibits a gapped Haldane state as its ground state, demonstrating the flexibility of ground-state topology in quantum spin systems, which is dependent on the spin size. Consequently, mixed-spin systems comprising different spin sizes offer an intriguing platform for studying unconventional quantum many-body phenomena that reflect quantum topology. Mixed-spin Heisenberg chains composed of spin $\frac{1}{2}$ and spin S ($S \geq 1$) have been extensively studied theoretically as fundamental systems. The ground states of these systems are described as quantum ferrimagnetic states, as predicted by the Lieb-Mattis (LM) theorem [1]. Topological arguments have also suggested the emergence of quantized magnetization plateaus in these systems [2]. Several bimetallic compounds that form mixed-spin chains have been reported [3–8]. Moreover, recent studies have successfully realized the LM plateau in a verdazyl-based salt with FeCl_4^- anion, forming a mixed-spin- $(\frac{1}{2}, \frac{5}{2})$ chain [9–11].

Theoretical investigations have extensively explored various spin lattices in mixed-spin two-dimensional (2D) systems, particularly emphasizing the Ising property arising from the on-site anisotropy [12–16]. Experimentally, metal-organic frameworks formulated as $(\text{A})[\text{M}^{\text{II}}\text{M}^{\text{III}}(\text{ox})_3]$ have emerged as well-known candidates. Here, M^{II} and M^{III} represent two- and three-valent transition metal atoms, respectively. These

frameworks consist of honeycomb-based bimetallic sheets with an alternating arrangement of M^{II} and M^{III} atoms [17–22]. However, the magnetic properties in the phases induced by an external magnetic field, which reflect different spin sizes, have not been thoroughly investigated due to the limited number of candidates capable of forming a variety of spin lattices. Therefore, unraveling the magnetic properties induced by a magnetic field is crucial for comprehending the quantum behavior that originates from mixed-spin 2D systems.

In our recent work, we have successfully developed a material design strategy using organic radicals to create mixed-spin 2D systems. By treating triphenyl verdazyl radicals as form-designed radicals, we have achieved stable radicals with a spin- $\frac{1}{2}$ configuration, enabling the realization of unconventional spin- $\frac{1}{2}$ Heisenberg systems [23–30]. By transforming form-designed radicals into ligand structures, we introduced metal-radical couplings and magnetic anisotropy into spin model designs using radical-based complexes with $3d$ transition metals [31–37]. Notably, by utilizing nondirect coordination to the radical center, we achieved metal-radical exchange couplings on the order of several kelvin, resulting in the formation of mixed-spin systems comprising intermolecular $\pi - \pi$ stacking and intramolecular $\pi - d$ couplings [38–41]. For example, in the case of $(p\text{-Py-V})_2[\text{Mn}(\text{hfac})_2]$, we observed the formation of a mixed-spin- $(\frac{1}{2}, \frac{1}{2}, \frac{5}{2})$ ferromagnetic chain, where spin- $\frac{1}{2}$ radicals and spin- $\frac{5}{2}$ Mn^{2+} ions are involved. This marked the first observation of thermodynamic properties that are universal to mixed-spin ferromagnetic chains [39]. Similarly, complexes with Co^{2+} ions, such as $(p\text{-Py-V-}p\text{-Br})_2[\text{Co}(\text{hfac})_2]$ [40] and $(p\text{-Py-V-}p\text{-F})_2[\text{Co}(\text{hfac})_2]$ [41], exhibit mixed-spin systems with Ising-like exchange interactions. These systems consist of isotropic spin- $\frac{1}{2}$ radicals and anisotropic spin- $\frac{1}{2}$ Co^{2+} ions,

*Corresponding author: h_yamaguchi@omu.ac.jp

owing to the presence of spin-orbit coupling in the Co^{2+} ions. Furthermore, for $(p\text{-Py-V-}p\text{-F})_2[\text{Co}(\text{hfac})_2]$, the interplay of intermolecular and intramolecular interactions between two distinct spin sites forms a ladder-based 2D spin model. This demonstrates the effectiveness of forming mixed-spin 2D systems using complexes incorporating form-designed radicals.

In this study, we successfully synthesized $(p\text{-Py-V-}p\text{-F})_2[\text{Ni}(\text{hfac})_2]$ ($p\text{-Py-V-}p\text{-F} = 3\text{-(4-pyridinyl)-1-(4-fluorophenyl)-5-phenylverdazyl}$, $\text{hfac} = 1,1,1,5,5,5\text{-hexafluoro-2,4-pentanedione}$), which is a Ni-verdazyl complex. Molecular orbital (MO) calculations revealed the formation of a mixed-spin 2D lattice consisting of spin $\frac{1}{2}$ and spin 1. The magnetic susceptibility confirmed the presence of a spin- $\frac{1}{2}$ singlet dimer and the AFM behavior originating from spin 1. The magnetization curve displayed a $\frac{1}{2}$ plateau, representing the full polarization of spin 1 accompanied by the remaining spin- $\frac{1}{2}$ singlet dimer. The specific heat exhibits a distinct upturn below approximately 2.3 K at $H = 0$, indicating a phase transition signal. Quantum Monte Carlo (QMC) analysis further confirmed that the increase in the magnetization curve after the $\frac{1}{2}$ plateau phase primarily reflected the magnetic behavior associated with an effective spin- $\frac{1}{2}$ ladder composed of radicals. In the low-field region, where spin- $\frac{1}{2}$ forms a nonmagnetic singletlike state, the magnetic properties below the plateau phase are primarily attributed to the residual spin 1, which forms a spin-1 AFM chain through effective interactions.

II. EXPERIMENT

$p\text{-Py-V-}p\text{-F}$ was synthesized following a conventional procedure for producing verdazyl radicals [42]. A solution of $\text{Ni}(\text{hfac})_2 \cdot 2\text{H}_2\text{O}$ (170.2 mg, 0.36 mmol) in 10 ml of heptane was refluxed at 60 °C. Subsequently, a solution of $p\text{-Py-V-}p\text{-F}$ (199.4 mg, 0.60 mmol) in 4 ml of CH_2Cl_2 was slowly added, and the resulting mixture was stirred for 1 h. After cooling the mixed solution to room temperature, the dark-green crystalline solid of $(p\text{-Py-V-}p\text{-F})_2[\text{Ni}(\text{hfac})_2]$ was separated by filtration and washed with heptane. Single crystals were obtained by recrystallizing from a mixed solvent of CH_2Cl_2 and ethanol at 10 °C.

The x-ray intensity data were collected using a Rigaku XtaLAB Synergy-S instrument. The crystal structures were determined using a direct method using SIR2004 [43] and refined using the SHELXL97 crystal structure refinement program [44]. Anisotropic and isotropic thermal parameters were employed for nonhydrogen and hydrogen atoms, respectively, during the structure refinement. The hydrogen atoms were positioned at their calculated ideal positions. Magnetization measurements were conducted using a commercial superconducting quantum interference device magnetometer (MPMS-XL, Quantum Design). The diamagnetic contribution, determined using Pascal's method, was subtracted from the experimental data. High-field magnetization in pulsed magnetic fields was measured using a nondestructive pulse magnet at the Institute for Solid State Physics, University of Tokyo. Specific heat measurements were performed using a commercial calorimeter (PPMS, Quantum Design) employing a thermal relaxation method. All the experiments utilized small, randomly oriented single crystals.

MO calculations were conducted using the GAUSSIAN09 software package, employing the UB3LYP method for broken-symmetry hybrid density functional theory calculations. The intermolecular calculations utilized the 6-31G basis set, while the intramolecular calculations employed the 6-31G(d,p) basis set. The convergence criterion of 10^{-8} hartree was set for the calculations. To estimate the exchange interactions, we employed a conventional evaluation scheme [45].

The QMC code employed in this study is based on a directed loop algorithm with a stochastic series expansion representation [46]. The calculations were carried out for a system size of $N = 1728$ under periodic boundary conditions, where N represents the number of particles in the system. The absence of significant size-dependent effects was confirmed. All the calculations were performed using the ALPS software package [47,48]. To avoid the difficulty of calculations with site-dependent g values, we used a uniform normalized g value. Regarding the magnetic susceptibility ($\chi = M/H$), the calculated results were calibrated using the respective g values to account for the predominant contributions from spin $\frac{1}{2}$ and spin 1 in the high- and low-temperature regions, respectively. For the magnetic susceptibility, the calibration was performed using a boundary at approximately 10 K, and the χT values in the high-temperature range were adjusted to achieve a smooth connection with the calibrated results. Similarly, for the magnetization curve, the calculated results were calibrated using the corresponding g values, considering the predominant contributions from spin $\frac{1}{2}$ and spin 1 in the high- and low-field regions, respectively. The calibration was performed using the plateau phase as the boundary, and subsequently, the magnetization in the high-field region was adjusted to ensure a seamless connection with the calibrated results.

III. RESULTS

A. Crystal structure and spin model

Figure 1(a) displays the molecular structure of $(p\text{-Py-V-}p\text{-F})_2[\text{Ni}(\text{hfac})_2]$. The verdazyl radicals, $p\text{-Py-V-}p\text{-F}$, and Ni^{2+} ions possess spin values of $\frac{1}{2}$ and 1, respectively. The crystallographic parameters are provided in Table I, revealing that the crystal structure is isomorphic to that of $(p\text{-Py-V-}p\text{-F})_2[\text{Co}(\text{hfac})_2]$ [41]. The Ni^{2+} ion coordinates with two $p\text{-Py-V-}p\text{-F}$ ligands, resulting in an octahedral coordination environment. The two radicals in the molecule are equivalent in terms of crystallography, owing to the presence of an inversion center at the Ni atom position. Table II lists the bond lengths and angles relevant to the Ni atoms. Through MO calculations performed on $p\text{-Py-V-}p\text{-F}$, it was determined that approximately 64% of the total spin density resides in the central ring consisting of four N atoms. The phenyl and fluorophenyl rings directly attached to the central N atoms contribute approximately 16% and 12% of the spin density, respectively. The pyridine ring, which lacks a direct connection to the N atom, accounts for less than 8% of the spin density. MO calculations were further employed to assess the dominant exchange interactions. As a result, two primary intermolecular AFM interactions between the radicals were identified. Their values are evaluated as $J_{V1}/k_B = 92$ K and $J_{V2}/k_B = 10$ K, defined within the

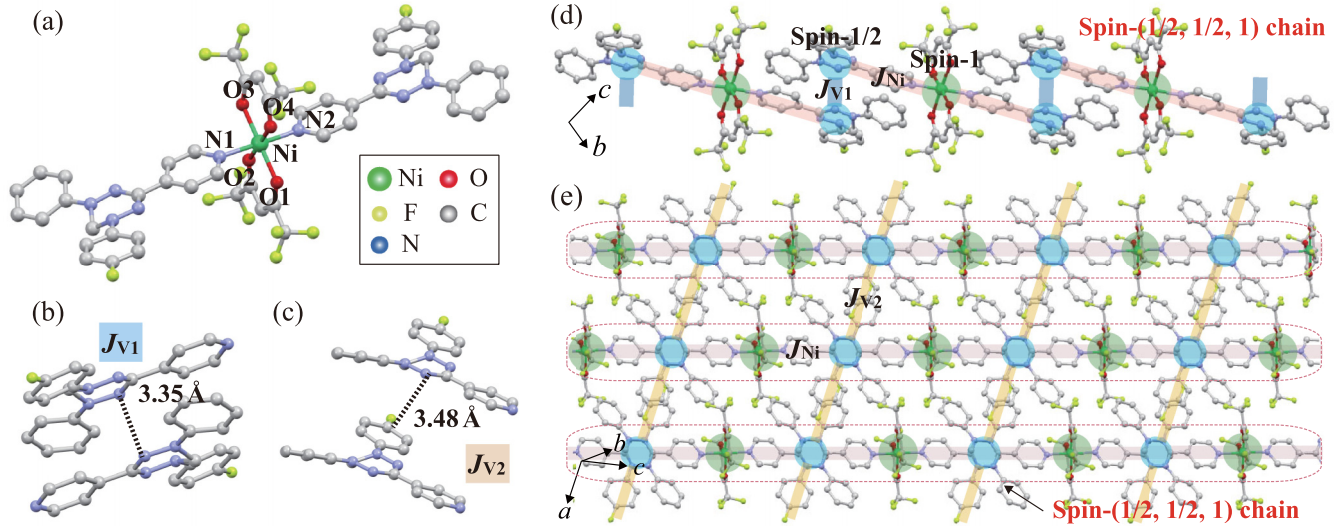


FIG. 1. (a) Molecular structure of $(p\text{-Py-V-}p\text{-F})_2[\text{Ni}(\text{hfac})_2]$. The hydrogen atoms have been omitted for clarity. Molecular pairs associated with the exchange interactions of (b) J_{V1} and (c) J_{V2} . The dashed lines indicate N-N and N-C short contacts. Crystal structure forming (d) the mixed-spin- $(\frac{1}{2}, \frac{1}{2}, 1)$ chain and (e) the mixed-spin 2D lattice with interchain couplings. The blue and green nodes represent the spin $\frac{1}{2}$ of the radical and spin 1 of the Ni atom. The thick lines represent the exchange interactions J_{V1} , J_{V2} , and J_{Ni} . The broken line encloses the molecules comprising each mixed-spin- $(\frac{1}{2}, \frac{1}{2}, 1)$ chain structure.

Heisenberg spin Hamiltonian, given by $\mathcal{H} = J_n \sum_{\langle i,j \rangle} s_i \cdot s_j$, where $\sum_{\langle i,j \rangle}$ denotes the sum over neighboring spin pairs. The $p\text{-Py-V-}p\text{-F}$ pair associated with J_{V1} is related by an inversion symmetry and has an N-N short contact of 3.35 Å, as shown in Fig. 1(b), which yields a large overlap of MOs. Regarding J_{V2} , the corresponding $p\text{-Py-V-}p\text{-F}$ pair exhibits translational symmetry and features a short N-C contact of 3.48 Å, as depicted in Fig. 1(c). These molecular pairs are equivalent to those observed in $(p\text{-Py-V-}p\text{-F})_2[\text{Co}(\text{hfac})_2]$, and similar values are obtained through MO calculations [41]. Notably, the MO calculation also indicates a relatively strong intramolecular interaction between the radical and

the Ni spins, evaluated as $J_{Ni}/k_B = 21$ K. Consequently, the compound is considered to form a mixed-spin- $(\frac{1}{2}, \frac{1}{2}, 1)$ chain along the $b + c$ direction through J_{V1} and J_{Ni} , as illustrated in Fig. 1(d). The spin chains are then coupled by J_{V2} , as shown in Fig. 1(e), resulting in a mixed-spin 2D lattice, as presented in Fig. 2. The presence of nonmagnetic hfac moieties between the 2D structures is expected to enhance the two-dimensionality of the spin system. From a topological perspective, this spin lattice consists of distorted squares and hexagons, thus forming a square-honeycomb lattice.

B. Magnetic and thermodynamic properties

Figure 3 depicts the temperature dependence of the magnetic susceptibility χ at 0.1 T, exhibiting a broad peak around 2.5 K. In the inset of Fig. 3, the temperature dependence of χT reveals a two-step decrease as the temperature is lowered. The initial decrease of χT from 300 K to approximately 10 K is attributed to the formation of an $s = \frac{1}{2}$ singlet dimer

TABLE I. Crystallographic data for $(p\text{-Py-V-}p\text{-F})_2[\text{Ni}(\text{hfac})_2]$.

Formula	$\text{C}_{48}\text{H}_{32}\text{NiF}_{14}\text{N}_{10}\text{O}_4$
Crystal system	Triclinic
Space group	$P\bar{1}$
Temperature (K)	100
a (Å)	9.0909(5)
b (Å)	11.1471(7)
c (Å)	13.8808(6)
α (deg)	110.130(5)
β (deg)	91.083(4)
γ (deg)	112.554(5)
V (Å ³)	1201.10(11)
Z	1
D_{calc} (g cm ⁻³)	1.573
Total reflections	2969
Reflection used	2648
Parameters refined	349
R [$I > 2\sigma(I)$]	0.0794
R_w [$I > 2\sigma(I)$]	0.2242
Goodness of fit	1.136
CCDC	2280586

TABLE II. Bond distances (Å) and angles (deg) related to the Ni atom for $(p\text{-Py-V-}p\text{-F})_2[\text{Ni}(\text{hfac})_2]$.

Ni-N1	2.07	O1-Ni-O2	90.9
Ni-N2	2.07	O2-Ni-O3	89.1
Ni-O1	2.04	O3-Ni-O4	90.9
Ni-O2	2.05	O4-Ni-O1	89.1
Ni-O3	2.04	N1-Ni-O4	91.4
Ni-O4	2.05	O4-Ni-N2	88.7
		N2-Ni-O2	91.4
		O2-Ni-N1	88.7
		N1-Ni-O3	90.4
		O3-Ni-N2	89.6
		N2-Ni-O1	90.4
		O1-Ni-N1	89.6

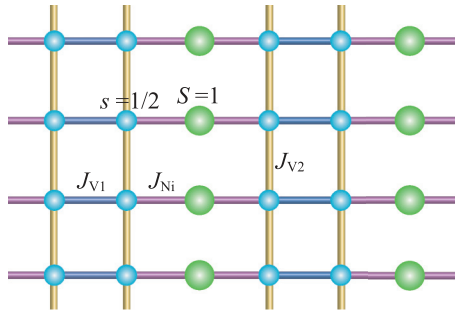


FIG. 2. Mixed-spin 2D lattice composed of J_{V1} , J_{V2} , and J_{Ni} , where s and S represent the spins on the radical and Ni^{2+} ion, respectively. The loops composed of $J_{V1} - J_{V2} - J_{V1} - J_{V2}$ and $J_{Ni} - J_{V2} - J_{Ni} - J_{Ni} - J_{V2} - J_{Ni}$ correspond to distorted square and hexagon in a square-honeycomb lattice, respectively.

coupled by the strong AFM interaction J_{V1} . Subsequently, the further decrease of χT in the lower-temperature region indicates AFM behavior originating from the residual Ni spins with $S = 1$.

Figure 4(a) shows the magnetization curve at 1.5 K in pulsed magnetic fields. A $\frac{1}{2}$ plateau in the magnetization is observed for fields ranging from approximately 17 and 42 T. This plateau indicates the full polarization of $S = 1$, and the magnetic field at the end of the plateau corresponds to the energy gap associated with the $s = \frac{1}{2}$ singlet dimer, considering the energy scale of the effective interactions evaluated from the observed χ . The value of $2.30/\text{f.u.}$ at the plateau corresponds to the average g value of $S = 1$, namely, $g_{Ni} = 2.30$. Because the organic radicals with $s = \frac{1}{2}$ typically have an isotropic g value of 2.00, the saturation magnetization of the current system is expected to be $4.30\mu_B/\text{f.u.}$ Figure 4(b) displays the field derivative of the magnetization curve (dM/dH)

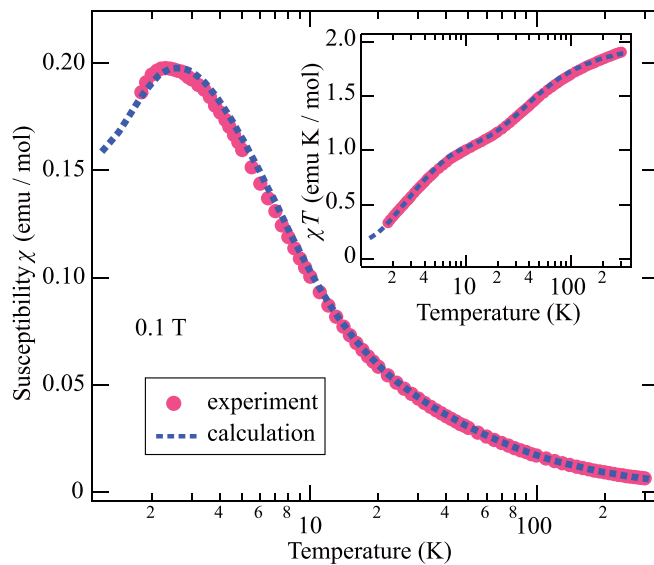


FIG. 3. (a) Temperature dependence of magnetic susceptibility ($\chi = M/H$) of $(p\text{-Py-V-}p\text{-F})_2[\text{Ni}(\text{hfac})_2]$ at 0.1 T. The inset shows corresponding χT values. The broken lines represent the calculated results for the mixed-spin 2D lattice with $\alpha = J_{V2}/J_{V1} = 0.170$ and $\beta = J_{Ni}/J_{V1} = 0.216$ by using the QMC method.

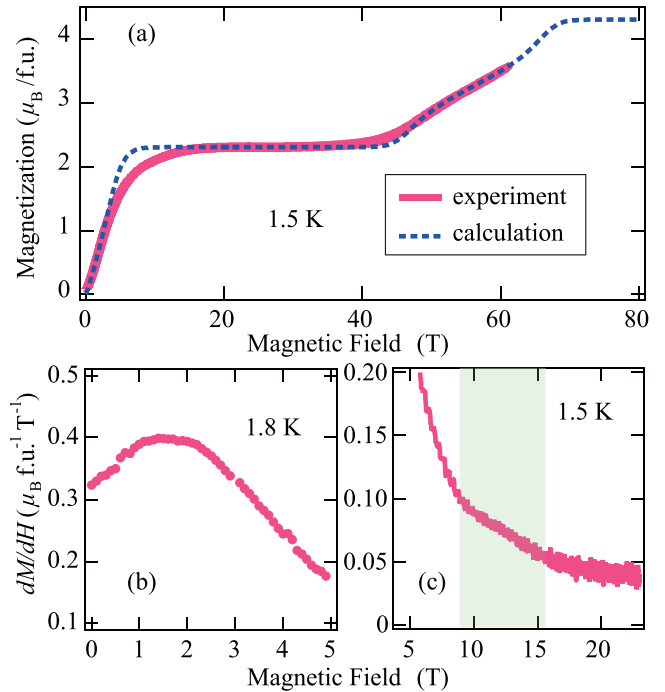


FIG. 4. (a) Magnetization curve of $(p\text{-Py-V-}p\text{-F})_2[\text{Ni}(\text{hfac})_2]$ at 1.5 K. The broken line represents the calculated results for the mixed-spin 2D lattice with $\alpha = J_{V2}/J_{V1} = 0.170$ and $\beta = J_{Ni}/J_{V1} = 0.216$ by using the QMC method. The field derivatives of the magnetization curve (dM/dH) in (b) the low-field region and (c) near the onset of the plateau. The colored area represents the intermediate phase with an anomalous change.

in a static field at 1.8 K. It approaches a finite value near $H = 0$, indicating a gapless ground state. In the field region close to the onset of the plateau, an anomalous change in dM/dH is observed, as shown in Fig. 4(c). This behavior suggests the presence of an intermediate phase below the plateau phase.

Figure 5 shows the temperature dependence of specific heat. We observe a monotonically decreasing trend as the temperature decreases, with a clear upturn below approximately 2.3 K at $H = 0$. This upturn disappears when applying magnetic fields. The presence of this upturn suggests the occurrence of a phase transition to an AFM-ordered state of S_{Ni} spins in the lower-temperature region. Therefore, all experimental results measured in the present study exhibit the paramagnetic behavior above the phase transition temperature. The observed specific heat behavior is also in line with the expected gapless behavior inferred from the magnetization measurements. The phase transition temperature to an AFM-ordered state typically decreases with increasing magnetic field due to the polarization of the spins. Accordingly, the disappearance of the phase transition signal by applying field is considered to correspond to a fully polarized state of S_{Ni} spins in the low-temperature region, which is consistent with the appearance of the plateau phase with a spin gap.

IV. ANALYSES AND DISCUSSION

The magnetic properties of the spin model were investigated based on the results of MO calculations. The dominant

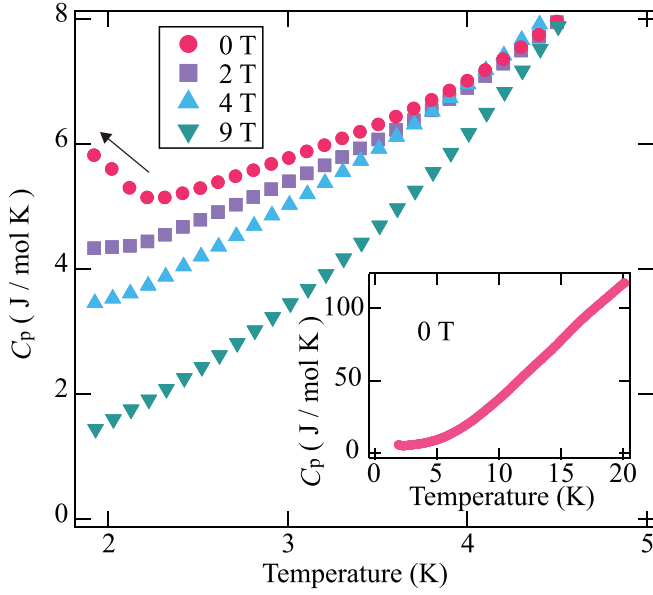


FIG. 5. Temperature dependence of the specific heat C_p of $(p\text{-Py-V-}p\text{-F})_2[\text{Ni}(\text{hfac})_2]$ at various magnetic fields. The arrow indicates the increase toward the phase transition signal. The inset shows C_p at zero field with the expanded temperature regime.

AFM interactions, J_{V1} , J_{V2} , and J_{Ni} , give rise to a mixed-spin square-honeycomb lattice, as shown in Fig. 2. To further analyze the system, magnetic susceptibility and magnetization curves were calculated using the QMC method, considering the parameters $\alpha = J_{V2}/J_{V1}$ and $\beta = J_{\text{Ni}}/J_{V1}$. The Heisenberg spin Hamiltonian was assumed,

$$\mathcal{H} = J_{V1} \sum_{ij} s \cdot s_j + J_{V2} \sum_{kl} s_k \cdot s_l + J_{\text{Ni}} \sum_{mn} s_m \cdot s_n - g_V \mu_B H \sum_i s_i - g_{\text{Ni}} \mu_B H \sum_i S_i, \quad (1)$$

where s and S represent the spin- $\frac{1}{2}$ and spin-1 operators, respectively. The g values were determined from the experimental magnetization data as $g_V = 2.00$ for the organic radicals and $g_{\text{Ni}} = 2.30$ for the Ni ions.

Initially, we note that the $\frac{1}{2}$ magnetization plateau represents the full polarization of the $S = 1$, where there are no additional degrees of freedom to modify the ground state. Therefore, the behavior observed in the magnetization curve beyond the $\frac{1}{2}$ plateau mainly reflects the magnetic properties of the spin ladder formed by J_{V1} and J_{V2} , which create a rung-singlet state with an energy gap. Figure 6(a) shows the high-field segment of the calculated magnetization curves at 1.5 K for representative values of α while keeping β fixed, where the magnetic moment of the fully polarized $S = 1$ is added. The magnetization curve for each α was scaled to have the same energy scale by adjusting the value of J_{V1} . As a result, identical intermediate fields toward saturation were obtained. Consequently, the values of J_{V1}/k_B were determined as 59 K ($\alpha = 0.10$), 57 K ($\alpha = 0.15$), 56 K ($\alpha = 0.20$), 55 K ($\alpha = 0.25$), and 54 K ($\alpha = 0.30$). As α increases, the one-dimensionality of the lattice formed by J_{V1} and J_{V2}

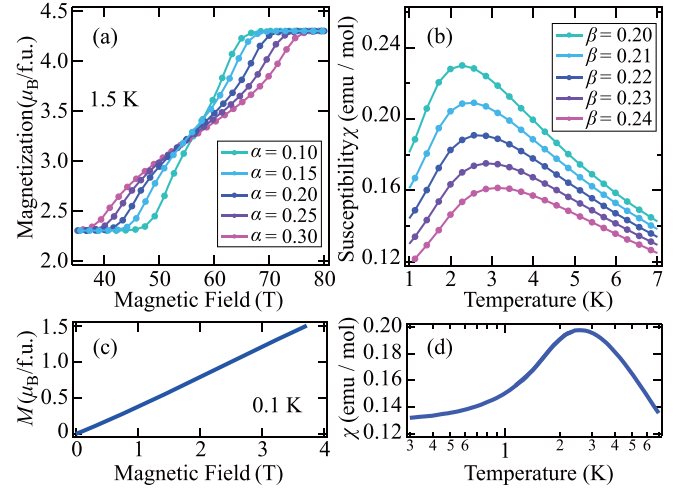


FIG. 6. (a) Calculated magnetization curves at 1.5 K for the mixed-spin 2D lattice with the representative values of $\alpha = J_{V2}/J_{V1}$ with fixed $\beta = J_{\text{Ni}}/J_{V1} = 0.216$. (b) Calculated magnetic susceptibilities for the mixed-spin 2D lattice with the representative values of β with fixed $\alpha = 0.170$. (c) The magnetization curve at 0.1 K and (d) low-temperature χ calculated with $\alpha = 0.170$ and $\beta = 0.216$.

becomes more prominent, resembling a uniform spin ladder. Consequently, the field region corresponding to the gapless TLL-like phase expands, leading to a decrease in the slope of the magnetization curve, as shown in Fig. 6(a).

In the low-field and low-temperature regions, the magnetic behavior is predominantly determined by the residual $S = 1$ spins, as the $s = \frac{1}{2}$ AFM dimer through J_{V1} is considered to be in a nonmagnetic singletlike state. The effective interactions between the $S = 1$ spins arise from the triplet excited states of the $s = \frac{1}{2}$ AFM dimer. By employing second-order perturbation theory for J_{V2} and J_{Ni} in the spin Hamiltonian, the most significant effective interaction arises from $J_{\text{Ni}} - J_{V1} - J_{\text{Ni}}$ [25], resulting in the formation of an effective $S = 1$ AFM chain. Therefore, the broad peak of χ observed in the low-temperature region primarily originates from the AFM contribution of the effective $S = 1$ chain, leading to a pronounced dependence on β , as shown in Fig. 6(b). For each β , the value of J_{V1} was fixed based on the analysis of the magnetization curve. As β increases, the strength of the effective interactions between the $S = 1$ spins becomes enhanced, leading to larger temperature shifts in the peak temperature and reductions in the peak value.

Based on the parameter values $\alpha = 0.170$ and $\beta = 0.216$ with $J_{V1}/k_B = 57$ K, which showed good agreement between the experimental data and calculations, as depicted in Figs. 3 and 4(a), we can confirm that the evaluated values of J_{V1} and J_{V2} are close to those determined in the Co complex with similar molecular orbital overlaps [41]. Moreover, the values of α and β are consistent with those evaluated from the MO calculations. With these parameters, we can further investigate the presence of a spin gap associated with the effective interactions forming the $S = 1$ AFM chain. The results demonstrate a finite slope in the magnetization curve at low temperatures and a finite value of low-temperature χ , indicating a gapless ground state in the system [shown in Figs. 6(c)

and 6(d)]. These findings suggest that the $S = 1$ Haldane state with a spin gap expected from the effective one-dimensional (1D) interaction is destabilized by weak interchain couplings. Although the 1D correlations are expected to be dominant in the low-temperature region, the ground state has gapless AFM character due to the 2D nature of the spin system. Additionally, when comparing the calculated and experimental magnetization curves, a relatively large deviation is observed near the onset of the plateau. It is important to note that in the present analysis, we assumed a Heisenberg spin Hamiltonian with only the bilinear term. However, the peculiar behavior observed in this region, as well as the anomalous change in dM/dH , could be attributed to on-site anisotropy and/or biquadratic exchange interactions associated with the $S = 1$ spins.

V. SUMMARY

We successfully synthesized the verdazyl-based complex (*p*-Py-V-*p*-F)₂[Ni(hfac)₂]. MO calculations indicated the formation of a mixed-spin 2D lattice consisting of spin $\frac{1}{2}$ and spin 1. From a topological perspective, the spin lattice is equivalent to a square-honeycomb lattice. The temperature dependence of the magnetic susceptibility shows the formation of a spin- $\frac{1}{2}$ singlet dimer from 300 K to approximately 10 K, followed by AFM behavior originating from spin 1 in the low-temperature region. The magnetization curve exhibited a $\frac{1}{2}$ plateau corresponding to the full polarization of spin 1, with the remaining spin- $\frac{1}{2}$ singlet dimer. The specific heat indicated a clear upturn

associated with a phase transition signal below approximately 2.3 K at $H = 0$. In the low-field and low-temperature regions, the magnetic behavior was primarily attributed to the spin-1 with effective interactions forming a spin-1 AFM chain. Moreover, by comparing the calculated and experimental results of the magnetization curves, a relatively large deviation was observed near the onset of the plateau, which could be associated with the observed anomalous change in dM/dH . This peculiar behavior in the mixed-spin 2D system is thought to stem from on-site anisotropy and/or biquadratic exchange interactions attributed to spin 1.

These findings clearly establish that the current complex manifests as a mixed-spin 2D lattice and showcases the quantum phenomena associated with such mixed spins. The incorporation of various molecular structures and transition metals offers the potential to generate a wide range of mixed-spin systems consisting of both spin- $\frac{1}{2}$ and integer spins, along with on-site anisotropy. This research is expected to inspire further investigations into quantum many-body phenomena arising from mixed spins.

ACKNOWLEDGMENTS

We thank K. Okamoto and T. Tonegawa for valuable discussions. This research was partly supported by KAKENHI (Grants No. 23K13065 and No. 23H01127). A part of this work was performed under the interuniversity cooperative research program of the joint-research program of ISSP, The University of Tokyo.

-
- [1] E. Lieb and D. Mattis, *J. Math. Phys.* **3**, 749 (1962).
 - [2] M. Oshikawa, M. Yamanaka, and I. Affleck, *Phys. Rev. Lett.* **78**, 1984 (1997).
 - [3] M. Verdaguer, A. Gleizes, J. P. Renard, and J. Seiden, *Phys. Rev. B* **29**, 5144 (1984).
 - [4] A. Gleizes and M. Verdaguer, *J. Am. Chem. Soc.* **103**, 7373 (1981).
 - [5] O. Kahn, Y. Pei, M. Verdaguer, J. P. Renard, and J. Sletten, *J. Am. Chem. Soc.* **110**, 782 (1988).
 - [6] P. J. Van Koningsbruggen, O. Kahn, K. Nakatani, Y. Pei, J. P. Renard, M. Drillon, and P. Legoll, *Inorg. Chem.* **29**, 3325 (1990).
 - [7] M. Hagiwara, K. Minami, Y. Narumi, K. Tatani, and K. Kindo, *J. Phys. Soc. Jpn.* **67**, 2209 (1998).
 - [8] M. Hagiwara, Y. Narumi, K. Minami, K. Tatani, and K. Kindo, *J. Phys. Soc. Jpn.* **68**, 2214 (1999).
 - [9] H. Yamaguchi, T. Okita, Y. Iwasaki, Y. Kono, N. Uemoto, Y. Hosokoshi, T. Kida, T. Kawakami, A. Matsuo, and M. Hagiwara, *Sci. Rep.* **10**, 9193 (2020).
 - [10] H. Yamaguchi, Y. Iwasaki, Y. Kono, T. Okita, A. Matsuo, M. Akaki, M. Hagiwara, and Y. Hosokoshi, *Phys. Rev. B* **102**, 060408(R) (2020).
 - [11] H. Yamaguchi, T. Okita, Y. Iwasaki, Y. Kono, Y. Hosokoshi, T. Kida, A. Matsuo, T. Kawakami, and M. Hagiwara, *J. Phys. Soc. Jpn.* **90**, 064707 (2021).
 - [12] J. Strečka and M. Jaščur, *Phys. Rev. B* **70**, 014404 (2004).
 - [13] J. Oitmaa, *Phys. Rev. B* **72**, 224404 (2005).
 - [14] J. Strečka, *Phys. A (Amsterdam, Neth.)* **360**, 379 (2006).
 - [15] J. Strečka, L. Čanová, and M. Jaščur, *Phys. Rev. B* **76**, 014413 (2007).
 - [16] M. Žukovič and A. Bobák, *Phys. Rev. E* **91**, 052138 (2015).
 - [17] Z. J. Zhong, N. Matsumoto, H. Ōkawa, and S. Kida, *Chem. Lett.* **19**, 87 (1990).
 - [18] H. Tamaki, Z. J. Zhong, N. Matsumoto, S. Kida, M. Koikawa, Y. Aihiwa, Y. Hashimoto, and H. Ōkawa, *J. Am. Chem. Soc.* **114**, 6974 (1992).
 - [19] S. Decurtins, S. W. Schmalte, H. R. Oswald, A. Linden, J. Ensling, P. Gülich, and A. Hauser, *Inorg. Chim. Acta* **216**, 65 (1994).
 - [20] C. Mathonière, C. J. Nuttall, S. G. Carling, and P. Day, *Inorg. Chem.* **35**, 1201 (1996).
 - [21] H. Ōkawa, A. Mishima, H. Yoshino, and M. Ohba, *Chem. Lett.* **47**, 444 (2018).
 - [22] H. Ōkawa, Y. Yoshida, K. Otsuka, and H. Kitagawa, *Inorg. Chem.* **59**, 623 (2020).
 - [23] H. Yamaguchi, K. Iwase, T. Ono, T. Shimokawa, H. Nakano, Y. Shimura, N. Kase, S. Kittaka, T. Sakakibara, T. Kawakami, and Y. Hosokoshi, *Phys. Rev. Lett.* **110**, 157205 (2013).
 - [24] K. Iwase, H. Yamaguchi, T. Ono, T. Shimokawa, H. Nakano, A. Matsuo, K. Kindo, H. Nojiri, and Y. Hosokoshi, *J. Phys. Soc. Jpn.* **82**, 074719 (2013).
 - [25] H. Yamaguchi, T. Okubo, K. Iwase, T. Ono, Y. Kono, S. Kittaka, T. Sakakibara, A. Matsuo, K. Kindo, and Y. Hosokoshi, *Phys. Rev. B* **88**, 174410 (2013).
 - [26] H. Yamaguchi, H. Miyagai, M. Yoshida, M. Takigawa, K. Iwase, T. Ono, N. Kase, K. Araki, S. Kittaka, T. Sakakibara,

- T. Shimokawa, T. Okubo, K. Okunishi, A. Matsuo, and Y. Hosokoshi, *Phys. Rev. B* **89**, 220402(R) (2014).
- [27] H. Yamaguchi, T. Okubo, S. Kittaka, T. Sakakibara, K. Araki, K. Iwase, N. Amaya, T. Ono, and Y. Hosokoshi, *Sci. Rep.* **5**, 15327 (2015).
- [28] H. Yamaguchi, Y. Tamekuni, Y. Iwasaki, and Y. Hosokoshi, *Phys. Rev. B* **97**, 201109(R) (2018).
- [29] H. Yamaguchi, Y. Sasaki, T. Okubo, M. Yoshida, T. Kida, M. Hagiwara, Y. Kono, S. Kittaka, T. Sakakibara, M. Takigawa, Y. Iwasaki, and Y. Hosokoshi, *Phys. Rev. B* **98**, 094402 (2018).
- [30] H. Yamaguchi, Y. Iwasaki, Y. Kono, T. Okubo, S. Miyamoto, Y. Hosokoshi, A. Matsuo, T. Sakakibara, T. Kida, and M. Hagiwara, *Phys. Rev. B* **103**, L220407 (2021).
- [31] H. Yamaguchi, Y. Shinpuku, T. Shimokawa, K. Iwase, T. Ono, Y. Kono, S. Kittaka, T. Sakakibara, and Y. Hosokoshi, *Phys. Rev. B* **91**, 085117 (2015).
- [32] H. Yamaguchi, Y. Shinpuku, Y. Kono, S. Kittaka, T. Sakakibara, M. Hagiwara, T. Kawakami, K. Iwase, T. Ono, and Y. Hosokoshi, *Phys. Rev. B* **93**, 115145 (2016).
- [33] H. Yamaguchi, M. Okada, Y. Kono, S. Kittaka, T. Sakakibara, T. Okabe, Y. Iwasaki, and Y. Hosokoshi, *Sci. Rep.* **7**, 16144 (2017).
- [34] N. Uemoto, Y. Kono, S. Kittaka, T. Sakakibara, T. Yajima, Y. Iwasaki, S. Miyamoto, Y. Hosokoshi, and H. Yamaguchi, *Phys. Rev. B* **99**, 094418 (2019).
- [35] Y. Kono, T. Okabe, N. Uemoto, Y. Iwasaki, Y. Hosokoshi, S. Kittaka, T. Sakakibara, and H. Yamaguchi, *Phys. Rev. B* **101**, 014437 (2020).
- [36] Y. Iwasaki, T. Okabe, N. Uemoto, Y. Kono, Y. Hosokoshi, S. Nakamura, S. Kittaka, T. Sakakibara, M. Hagiwara, T. Kawakami, and H. Yamaguchi, *Phys. Rev. B* **101**, 174412 (2020).
- [37] H. Yamaguchi, N. Uemoto, T. Okubo, Y. Kono, S. Kittaka, T. Sakakibara, T. Yajima, S. Shimono, Y. Iwasaki, and Y. Hosokoshi, *Phys. Rev. B* **104**, L060411 (2021).
- [38] H. Tsukiyama, S. Morota, S. Shimono, Y. Iwasaki, M. Hagiwara, Y. Hosokoshi, and H. Yamaguchi, *Phys. Rev. Mater.* **6**, 094417 (2022).
- [39] H. Yamaguchi, S. C. Furuya, S. Morota, S. Shimono, T. Kawakami, Y. Kusanose, Y. Shimura, K. Nakano, and Y. Hosokoshi, *Phys. Rev. B* **106**, L100404 (2022).
- [40] S. Morota, Y. Iwasaki, M. Hagiwara, Y. Hosokoshi, and H. Yamaguchi, *J. Phys. Soc. Jpn.* **92**, 054705 (2023).
- [41] H. Yamaguchi, Y. Tominaga, A. Matsuo, S. Morota, Y. Hosokoshi, M. Hagiwara, and K. Kindo, *Phys. Rev. B* **107**, 174422 (2023).
- [42] R. Kuhn, *Angew. Chem.* **76**, 691 (1964).
- [43] M. C. Burla, R. Caliendo, M. Camalli, B. Carrozzini, G. L. Casciarano, L. De Caro, C. Giacovazzo, G. Polidori, and R. Spagna, *J. Appl. Crystallogr.* **38**, 381 (2005).
- [44] G. M. Sheldrick, *SHELXL97, Program for Crystal Structure Determination* (University of Göttingen, Germany, 1997).
- [45] M. Shoji, K. Koizumi, Y. Kitagawa, T. Kawakami, S. Yamanaka, M. Okumura, and K. Yamaguchi, *Chem. Phys. Lett.* **432**, 343 (2006).
- [46] A. W. Sandvik, *Phys. Rev. B* **59**, R14157(R) (1999).
- [47] A. F. Albuquerque, F. Alet, P. Corboz, P. Dayal, A. Feiguin, L. Gamper, E. Gull, S. Gurtler, A. Honecker, R. Igarashi, M. Korner, A. Kozhevnikov, A. Lauchli, S. R. Manmana, M. Matsumoto, I. P. McCulloch, F. Michel, R. M. Noack, G. Pawłowski, L. Pollet *et al.*, *J. Magn. Magn. Mater.* **310**, 1187 (2007).
- [48] B. Bauer, L. D. Carr, A. Feiguin, J. Freire, S. Fuchs, L. Gamper, J. Gukelberger, E. Gull, S. Guertler, A. Hehn, R. Igarashi, S. V. Isakov, D. Koop, P. N. Ma, P. Mates, H. Matsuo, O. Parcollet, G. Pawłowski, J. D. Picon, L. Pollet *et al.*, *J. Stat. Mech.* (2011) P05001.